Applied Catalysis B: Environmental 248 (2019) 11–21

Contents lists available at ScienceDirect

Applied Catalysis B: Environmental

journal homepage: www.elsevier.com/locate/apcatb

Visible-light-driven photocatalytic disinfection of human adenovirus by a novel heterostructure of oxygen-doped graphitic carbon nitride and hydrothermal carbonation carbon

Chi Zhang[a], Mengyang Zhang[b], Yi Li[a,*], Danmeng Shuai[b]

[a] Key Laboratory of Integrated Regulation and Resource Development of Shallow Lakes, Ministry of Education, College of Environment, Hohai University, Xikang Road #1, Nanjing 210098, PR China

[b] Department of Civil and Environmental Engineering, The George Washington University, 800 22nd St NW Suite 3530, Washington DC 20052, United States

ARTICLE INFO

Keywords:
Photocatalysis
Z-scheme heterojunction
Graphitic carbon nitride
Hydrothermal carbonation carbon
Human adenovirus

ABSTRACT

Waterborne pathogenic viruses, with an ultra-small particle size of tens of nanometers, a high risk of causing disease, and strong persistence in natural environment and water treatment processes, pose a serious threat to human health. Here, a new class of metal-free heterojunction photocatalysts was developed by integrating oxygen-doped graphitic carbon nitride microspheres (O-g-C_3N_4) with hydrothermal carbonation carbon (HTCC) via a facile low-temperature solvothermal-hydrothermal approach for the inactivation of human adenovirus type 2 (HAdV-2). The sample of O-g-C_3N_4/HTCC-2 with a uniform coverage of HTCC, strong visible light absorption, and a narrow band gap exhibited the higher virucidal activity against highly resistant HAdV-2 under visible light irradiation, compared to HTCC, bulk g-C_3N_4, and O-g-C_3N_4. A titer of 10^5 MPN/mL viruses was completely inactivated within 120 min of photocatalysis, and viral inactivation efficiency was enhanced with the increase of water temperature from 4 to 37 °C, the decrease of pH from 8 to 5, or the presence of salinity (NaCl) and hardness (Ca^{2+}). Furthermore, the effectiveness for HAdV-2 inactivation in real drinking water and excellent photocatalyst stability of O-g-C_3N_4/HTCC-2 highlighted its promising potential for water disinfection in practice. The mechanism of enhanced virucidal performance of O-g-C_3N_4/HTCC was revealed, and it was because of enhanced charge separation by the formation of heterojunction in the photocatalyst. Besides, Z-scheme heterojunction was proposed to enable the production of $^{\cdot}OH$ as a strong antiviral agent in photocatalysis, in contrast to Type II heterojunction. Interestingly, $^{\cdot}OH$ rather than $^{\cdot}O_2^-$ dominated HAdV-2 inactivation, and it led to the rupture, distortion, and hole formation of viral capsid. In addition to the excellent photocatalytic performance of O-g-C_3N_4/HTCC for HAdV-2 inactivation, the photocatalyst exhibited negligible toxicity to a human cell line, suggesting the material is safe for water purification. Our study not only highlights the promising future of an emerging metal-free visible-light-responsive heterostructure of O-g-C_3N_4/HTCC for viral disinfection and an effective, sustainable, and safe water purification process, but also sheds light on the key photocatalyst properties and mechanisms that improve photocatalytic performance.

1. Introduction

Waterborne pathogens including bacteria, viruses, protozoa, and helminths in drinking water pose a significant threat to human health because these pathogens lead to serious infectious diseases or disease outbreaks. Among them, viruses with the smallest size around tens of nanometers have a low infectious dose and a high illness risk, e.g. exposure to only one rotavirus particle could lead to more than 30% of infectious probability [1,2], and thus the viruses attract great attention in water treatment and safe drinking water supply. However, conventional water treatment processes are not ideal or optimized for viral removal or inactivation. Viruses can easily pass through common physical barriers such as granular activated carbon filters in water treatment plants [3]. Membrane processes such as ultrafiltration, nanofiltration, and reverse osmosis can remove viruses effectively due to a larger viral particle size compared to the membrane pore size, but membrane filtration requires extensive energy and chemical consumption (e.g., membrane operation, cleaning, and antiscalant application). Moreover, viruses such as adenoviruses and rotaviruses are highly resistant to UV radiation in water disinfection [4–6]. Chemical

* Corresponding author.
E-mail address: envly@hhu.edu.cn (Y. Li).

https://doi.org/10.1016/j.apcatb.2019.02.009
Received 10 November 2018; Received in revised form 12 January 2019; Accepted 6 February 2019
Available online 07 February 2019
0926-3373/ © 2019 Elsevier B.V. All rights reserved.

disinfectants including free chlorine, chlorine dioxide, and ozone are effective for inactivating viruses, but along with the handling and storage of strong oxidants, complicated on-site generation of disinfectants, and potential formation of mutagenic and carcinogenic disinfection byproducts [2,7,8]. Therefore, there is a pressing need to develop an effective strategy for viral removal or inactivation in water treatment, and it will outperform the current water treatment paradigm to promote our sustainable water future.

Photocatalysis can utilize renewable solar energy for effective pathogen inactivation in water treatment via the generation of various reactive species (RS). Notably, viruses have been found with higher resistance to photocatalysis than most commonly used model pathogenic bacteria, due to a unique virion composition and structure [9,10]. To date, photocatalytic viral disinfection is still at its nascent stage for water treatment, in contrast to photocatalytic bacterial inactivation [11]. Recently, our group revealed that graphitic carbon nitride (g-C_3N_4), an emerging metal-free visible-light-responsive photocatalyst, exhibited good virucidal activity against bacteriophage MS2 under visible light irradiation for the first time [12]. g-C_3N_4 is an ideal photocatalyst for viral disinfection because it can be responsive under visible-light-irradiation, it is fabricated readily from earth-abundant precursors (e.g., urea), and it is stable and environmentally friendly with negligible toxicity [13]. In our pioneering work of viral disinfection by g-C_3N_4, a relatively long reaction duration was needed for complete viral inactivation even under an optimum experimental condition [14]. It calls for the need of developing a more reactive g-C_3N_4-based photocatalyst for viral disinfection and water treatment in practice.

One effective strategy to achieve desirable photocatalyst properties and improved photocatalytic performance is to construct a heterojunction between g-C_3N_4 and another semiconductor with a suitable band energy alignment. Hydrothermal carbonation carbon (HTCC), which is also metal-free and can be easily prepared by hydrothermal treatment of carbohydrates such as glucose, was recently found to act as a visible-light-responsive semiconductor [15]. It has been further doped with iodine for effective inactivation of *E. coli* bacteria, of which inactivation behavior and mechanism to photocatalysis are quite different from those of viruses due to their individual unique microbial composition, structure and resistance. Researchers have successfully coupled HTCC with semiconductive metal oxides to establish effective heterojunctions to enhance charge separation and performance in photocatalysis [16,17]. This attractive discovery has inspired us to couple HTCC with g-C_3N_4 to develop a novel metal-free heterojunction photocatalyst for effective viral inactivation. The combination of both materials will enable the production of effective and low-cost photocatalysts that can be synthesized via a facile and scalable manner, and it will also minimize the risks of metal leaching into the treated water because both materials are metal-free. Considering that the band energy alignment between HTCC and bare g-C_3N_4 is Type I straddling, which is always considered to impair RS production and photocatalytic performance [13], we selected O-doped g-C_3N_4 synthesized by a solvothermal method at low temperature [18] with suitable band energy levels for establishing a staggered heterojunction (Type II or Z-scheme), which is believed to significantly enhance photocatalytic performance. This novel heterojunction photocatalyst of O-g-C_3N_4/HTCC is expected to be of particular interest for virial disinfection in water treatment, due to the effectiveness of photocatalysis, metal-free nature of the material, and sustainability by using sunlight.

Herein, for the first time, a novel metal-free heterojunction photocatalyst (i.e. O-g-C_3N_4/HTCC) containing C, N, and O as the earth-abundant elements was designed and fabricated by a facile two-step approach (i.e. solvothermal-hydrothermal treatment at low temperature of 180 °C), and the photocatalyst was used for the disinfection of human adenovirus type 2 (HAdV-2) under visible light irradiation. Specifically, our study selected HAdV-2 as a probe virus for disinfection because it is a human virus in contrast to commonly used bacteriophage MS2 and is well-known to be resistant in UV disinfection, which can better evaluate the effectiveness of photocatalysis in disinfection for water treatment. The mass ratio of O-g-C_3N_4 and HTCC was optimized for developing the photocatalytic heterostructure of O-g-C_3N_4/HTCC, and photocatalyst properties were systematically characterized. The virucidal performance of O-g-C_3N_4/HTCC was explored under different reaction conditions that represent real water treatment practice. Furthermore, the dominant oxidative species and viral response in photocatalysis was elucidated by the RS analysis and transmission electron microscopic (TEM) characterization of HAdV-2 in disinfection, and the formation of a Z-scheme heterojunction in O-g-C_3N_4/HTCC to facilitate charge transfer was proposed based on the results of RS analysis and photoelectrochemical measurements. Lastly, negligible toxicity of O-g-C_3N_4/HTCC was observed in the viability evaluation of human alveolar epithelial cells (A549). Our study provides insights on the design and fabrication of an effective, sustainable, safe, and potentially scalable heterojunction photocatalyst that can harvest and utilize visible sunlight, and also sheds light on the performance and mechanism of photocatalytic viral inactivation, which can provide guidelines for implementing novel materials in water treatment practice.

2. Experimental

2.1. Synthesis of O-g-C_3N_4/HTCC microspheres

The O-g-C_3N_4 microspheres were prepared by a facile solvothermal method at low temperature according to the previous report of Wang et al. [18]. Typically, cyanuric chloride (15 mmol) and dicyandiamide (11 mmol) were dispersed in acetonitrile (60 mL). The mixture was stirred in a Teflon-lined autoclave (capacity of 100 mL) for 12 h, and then the autoclave was sealed and heated at 180 °C for 96 h. The obtained products were washed with distilled water and ethanol for several times, and dried in a vacuum oven at 60 °C for 12 h. Finally, the samples were collected and defined as O-g-C_3N_4.

The O-g-C_3N_4/HTCC microspheres were prepared by a facile hydrothermal method. Typically, O-g-C_3N_4 (1, 2, and 3 g, respectively) and glucose (8 g) were dissolved in distilled water (80 mL). The mixture was stirred in a Teflon-lined autoclave (capacity of 100 mL) for 6 h, and then the autoclave was sealed and heated at 180 °C for 10 h. The obtained products were washed with distilled water for several times, and dried in a vacuum oven at 60 °C for 12 h. Finally, the samples were collected and defined as O-g-C_3N_4/HTCC-1, O-g-C_3N_4/HTCC-2, and O-g-C_3N_4/HTCC-3, respectively.

2.2. Characterization

Scanning electron microscopic (SEM) images were obtained with a Hitachi SU8020 scanning electron microscope. Transmission electron microscopic (TEM) images were obtained with a Tecnai TF20 transmission electron microscope. X-ray diffraction (XRD) patterns were recorded by a Bruker AXS D8 diffractometer using Cu Kα radiation. Fourier-transform infrared (FTIR) spectra were recorded with a Perkin-Elmer Spectrum GX spectrometer. X-ray photoelectron spectroscopy (XPS) analysis was performed on a Thermo ESCALAB 250XI spectrometer. UV–vis diffuse reflectance spectra (DRS) were recorded with an Agilent Cary 300 spectrometer. Room-temperature photoluminescence (PL) spectra were obtained with a Hitachi F-7000 fluorescence spectrometer using an excitation wavelength of 325 nm.

2.3. Photocatalytic viral inactivation

Human adenovirus type 2 (ATCC VR-846) was propagated in a human lung carcinoma cell line A549 (ATCC CCL-185). Briefly, A549 cells were first maintained in the Ham's F-12 K medium supplemented with 10% fetal bovine serum (FBS) and 1% antibiotics of

penicillin-streptomycin-amphotericin B in an incubator with humidified air and 5% CO_2 at 37 °C. The adenovirus stock was next inoculated onto the A549 cellular monolayer with a confluence of 70%–80%. The medium was removed from the cell monolayer, and then the pre-warmed virus stock suspended in the Ham's F-12 K medium was added. The mixture was shaken homogeneously for 45 min in order to allow efficient adsorption of viruses on cells. After that, the mixture was cultured in the Ham's F-12 K medium supplemented with 2% FBS and 1% antibiotics of penicillin-streptomycin-amphotericin B in an incubator with humidified air and 5% CO_2 at 37 °C. The infected cells were collected after ~4 days and freeze-thawed for three times to release the viruses. The mixture was centrifuged at 1000*g* for 10 min at room temperature to separate cell debris. The supernatant was filtered through a 0.45 μm membrane for further purification. The filtrate was concentrated by a 100-kDa centrifugal membrane filter and washed by phosphate-buffered saline (PBS). Finally, the virus stock was stored at −80 °C until used. Viral titer was determined by the most probable number (MPN) method using 96-well microtiter plates [19–21].

The stock suspension of adenoviruses was diluted into 20 mL of deionized water in a 50 mL beaker to prepare a suspension with an initial viral concentration of 10^5 MPN/mL. After that, 3 mg of the freshly prepared photocatalysts was added for viral inactivation (i.e., photocatalyst loading of 0.15 g/L). The mixed suspension was kept at a room temperature and stirred throughout the disinfection experiment. The light source was a 7 W-white light emitting diode (LED) lamp with an illumination intensity of 40 mW/cm^2 to provide visible light ($\lambda > 400$ nm), and its light spectrum is presented in Fig. S1. And the corresponding experimental setups are also shown in Fig. S2.

The reactor was first left in the dark for 30 min to allow adsorption equilibrium of viruses on the photocatalyst. Adenoviruses were sampled at different time intervals of 0, 30, 60, 90, and 120 min during photocatalysis, and were immediately enumerated to avoid further inactivation. A viral solution without the photocatalyst was irradiated under the same light source as the light control, and a viral suspension with the photocatalyst but without irradiation was used as the dark control. The photocatalytic inactivation efficiency was reported as Log (C_t/C_0), where C_0 and C_t were the titer of adenoviruses before and after disinfection, respectively.

2.4. Photoelectrochemical measurements

Photoelectrochemical measurements were performed on a CHI1030B electrochemical workstation with a three-electrode cell. A saturated Ag/AgCl electrode, a platinum foil, and a fluorine tin oxide (FTO) electrode deposited with the photocatalyst sample were employed as the reference, counter, and working electrode, respectively. The working electrode was prepared by an electrophoretic deposition method. Photocurrent (PC) response and electrochemical impedance spectroscopy (EIS) were carried out in 0.1 M Na_2SO_4.

2.5. RS analysis

A series of photocatalytic disinfection experiments with the addition of scavengers to selectively quench RS were conducted to elucidate the mechanism of O-g-C_3N_4/HTCC-2 for viral inactivation. The scavengers included ammonium oxalate (0.5 mM) for h^+, potassium dichromate (0.025 mM) for e^-, TEMPOL (1 mM) for $^{\cdot}O_2^-$, and isopropanol (0.5 mM) for $^{\cdot}OH$, respectively, at which concentrations have no toxicity on viruses [10,12]. Nitroblue tetrazolium (NBT) (0.1 mM) was used to quantitatively determine the generation of $^{\cdot}O_2^-$ by measuring the decrease of the NBT concentration by a Hach DR-6000 UV–vis spectrophotometer. Terephthalic acid (TA) (3 mM in 10 mM NaOH solution) was used to quantitatively identify the production of $^{\cdot}OH$ by measuring the increase in 2-hydroxyterephthalic acid (2-HTA, a highly fluorescent product) concentration on a Hitachi F-7000 fluorescence spectrophotometer. Electron spin resonance spectroscopy (ESR) analysis of $^{\cdot}O_2^-$ and $^{\cdot}OH$ for further verification was recorded on a Bruker A300 spectrometer using 5,5-dimethyl-1-pyrroline *N*-oxide (DMPO) as the spin trap. Briefly, 2.5 mg of prepared samples was ultrasonically dispersed in 0.5 mL of methanol ($^{\cdot}O_2$-) or deionized water ($^{\cdot}OH$). And then 50 μL of the dispersion was mixed with 50 μL of 100 mM DMPO solution. Finally, the mixture was irradiated with visible light for 5 min and immediately analyzed by ESR.

2.6. Microscopic virus observation

Human adenovirus is a non-enveloped icosahedral virus with a double-stranded DNA genome, of which the diameter is in the range of 70–100 nm [22–24]. TEM images of adenoviruses stained by 2% uranyl acetate were obtained before and after photocatalytic disinfection by O-g-C_3N_4/HTCC-2 by a FEI Talos F200X transmission electron microscope at the voltage of 200 kV.

2.7. Cytotoxicity assay

The cytotoxic effects of HTCC, O-g-C_3N_4, and O-g-C_3N_4/HTCC-2 were evaluated by using A549 cells via an XTT assay [25–27]. Briefly, A549 cells were seeded in 96-well microplates with humidified air and 5% CO_2 at 37 °C for 24 h. The attached cells were then treated with different concentrations of photocatalysts (0, 10, and 150 μg/mL) for 24 h. 50 μL of XTT solution was next added to each well for an additional 4 h incubation at 37 °C. The sample absorbance was measured at 450 nm with a reference wavelength of 690 nm using a Synergy H1 Hybrid microplate reader. Finally, the cell viability was estimated as the percentage of the absorbance of photocatalyst-treated cells compared to the untreated cells used as a control.

3. Results and discussion

3.1. Photocatalyst characterization

HTCC sample presented an amorphous structure with no noticeable diffraction peak in the XRD analysis, while O-g-C_3N_4 sample exhibited a strong diffraction peak at 27.4° (d = 0.33 nm) (Fig. 1a), which is known as the (002) interlayer diffraction of graphite-like structures. The small (100) diffraction peak at ~13°, which is always observed in g-C_3N_4 materials, however it was not shown in the O-g-C_3N_4 sample, indicating a disordered packing of in-plane repeated units. This may suggest that O-g-C_3N_4 has an incompletely polymerized structure resulted from low-temperature solvothermal reactions, in contrast to a more completely polymerized structure of conventional g-C_3N_4 synthesized by high-temperature calcination (450–650 °C) [13,18]. In particular, a new diffraction peak at 10.6° (d = 0.83 nm) appeared after hydrothermal treatment, signifying the formation of a relatively regular in-plane connection of tri-*s*-triazine motifs, in agreement with melem structures [28–30]. However, a certain level of the structural disorders still existed due to the introduction of oxygen-containing groups to the composites. As expected, all O-g-C_3N_4/HTCC binary composites show the characteristic XRD pattern of both HTCC and O-g-C_3N_4.

FTIR characterization was conducted to examine the chemical structure and functional groups of the photocatalysts (Fig. 1b). On one hand, for HTCC, a series of typical polyfuran bands were observed, including the ones at 1623, 1444, and 1397 cm^{-1} arising from vibrational modes of the furan monomer. The bands at 1513, 1212 and 1025, and 799 cm^{-1} were assigned to C=C stretching and C−H bending vibrations in the furan ring, and α, α'-coupling of the carbon backbone in the polyfuran, respectively. In addition, the bands at 2926 and 1702 cm^{-1} were attributed to aliphatic C−H and C=O stretching vibrations, due to the opening of some furan rings in the polymer [15–17]. On the other hand, for O-g-C_3N_4, a series of characteristic vibrational modes of g-C_3N_4 were observed, including two regions of 3500-3000 and 1700-1200 cm^{-1} indicative of stretching vibrations of N−H and C−N

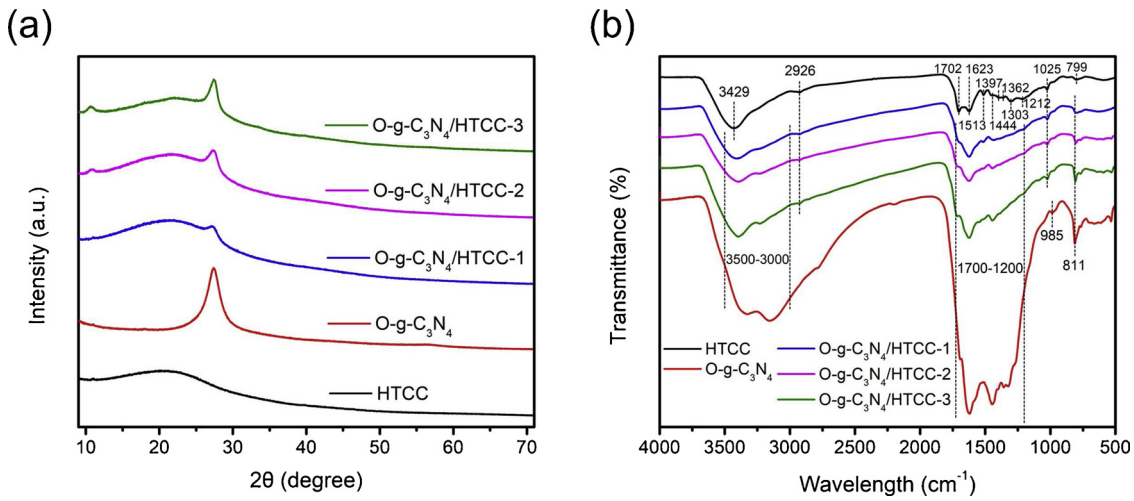

Fig. 1. (a) XRD patterns and (b) FTIR spectra of HTCC, O-g-C_3N_4, and different O-g-C_3N_4/HTCC samples.

heterocycles, respectively. The sharp peak at 811 cm^{-1} corresponded to a typical breathing mode of triazine units. Particularly, a new band at 985 cm^{-1} can be ascribed to the N—O stretching vibration owing to oxygen-functionalized carbon nitride [18,31]. As expected, some major bands of HTCC (e.g. 2926 and 1025 cm^{-1}) and O-g-C_3N_4 (e.g. 811 cm^{-1}) were still found in the composites of O-g-C_3N_4/HTCC, suggesting the combination of O-g-C_3N_4 and HTCC via a mild hydrothermal route maintained their main backbone structures.

The morphology of the photocatalysts were characterized by SEM and TEM, as shown in Fig. 2. HTCC presented aggregated spherical particles with a size of ~120 nm in diameter (Fig. 2a), while O-g-C_3N_4 exhibited non-aggregated microspheres with a size of ~2 μm in diameter (Fig. 2b). The O-g-C_3N_4 microspheres possessed a smooth surface, which was clearly seen in TEM images (Fig. 2f). After integrating O-g-C_3N_4 with HTCC, it could be obviously observed that O-g-C_3N_4 microspheres were covered by various amounts of HTCC in all composites (Figs. 2c-e). HTCC was found to be sporadically distributed on the surface of O-g-C_3N_4/HTCC-1 (Fig. 2c) but heavily aggregated on the surface of O-g-C_3N_4/HTCC-3 (Fig. 2e). A more uniform distribution of HTCC on the surface of O-g-C_3N_4/HTCC-2 was observed (Fig. 2d and g). The microsphere surface became rough (Fig. 2g), which might facilitate the interaction between the photocatalyst and viruses.

XPS was performed to investigate the chemical compositions and bonding environments of HTCC, O-g-C_3N_4, and O-g-C_3N_4/HTCC-2. As expected, all these photocatalysts were composed of C, N, and O elements (Fig. 3a). The N1s spectra of O-g-C_3N_4/HTCC-2 could be deconvoluted into three peaks (Fig. 3b), which are ascribed to sp^2-hybridized aromatic N bonded to C atoms (C═N—C, 398.8 eV), tertiary N bonded to C atoms (N-$(C)_3$, 399.7 eV), and amine functional groups (C—NH_x, 400.5 eV) originated from O-g-C_3N_4, respectively [32]. In the O1s spectra of the samples (Fig. 3c), two peaks in HTCC were assigned to C═O (532.3 eV) and C—O—C/C—OH (533.2 eV) [33], of which the binding energy shifted to lower values in O-g-C_3N_4/HTCC-2 composite. While for O-g-C_3N_4, in addition to the adsorbed water (532.9 eV), specially, the peak at 531.6 eV could be attributed to C_3-$^+$ N-O species formed by the oxidation of tertiary amines [18], which was also observed in the composite. The C1s spectra further confirmed the existence of C—C/C═C (284.5 eV), C—O—C/C—OH (285.7 eV), C═O/C—N /C≡N (287.1 eV), and the sp^2-hybridized C in the N-containing aromatic ring (C═N—C, 288.5 eV) in O-g-C_3N_4/HTCC-2 (Fig. 3d). The slight shift of binding energy in the composite might be resulted from the electronic interaction between O-g-C_3N_4 and HTCC with the formation of heterojunctions.

The optical property of the photocatalysts was surveyed by UV–vis DRS, as shown in Fig. 4. HTCC possessed an intrinsic semiconductor-like absorption in the wide region, and O-g-C_3N_4 displayed the absorption edge of photons at a longer wavelength (~650 nm) than most g-C_3N_4 (~450 nm), possibly because of the enhanced p-electron delocalization and in-plane packing in the conjugated system from the solvothermal process, and the reduced C—N bond length from O-doping [34,35]. After forming composites, all O-g-C_3N_4/HTCC samples exhibited stronger absorption across a broader spectrum (Fig. 4a). The absorption edge first red-shifted with an increasing amount of HTCC in the composite then blue-shifted with further increasing of HTCC. The difference of adsorption edge of the photocatalysts was also reflected in their band gap (Fig. 4b). The band gap of HTCC, O-g-C_3N_4, O-g-C_3N_4/HTCC-1, O-g-C_3N_4/HTCC-2, and O-g-C_3N_4/HTCC-3 was calculated to be 1.39, 1.88, 1.04, 0.95, and 1.16 eV, respectively. An excessive amount of HTCC could aggregate heavily on the surface of O-g-C_3N_4 and block incident light, which is detrimental for improving photocatalytic performance. In conclusion, all characterization results support the argument that O-g-C_3N_4 and HTCC were successfully combined to form composites.

3.2. Photocatalytic virucidal performance

The inactivation of HAdV-2 was used to evaluate the visible-light-driven photocatalytic antiviral activity of the as-prepared materials (Fig. 5a). Notably, adenoviruses are considered to be highly resistant to common treatment such as UV disinfection in comparison of other viral pathogens [36,37]. Almost no viral inactivation was found within 120 min in the dark or under visible light irradiation but without photocatalysts, demonstrating the high persistence of HAdV-2. The photocatalysts of a single component were assessed for HAdV-2 inactivation under visible light irradiation, however HTCC exhibited no photocatalytic antiviral activity and O-g-C_3N_4 only possessed moderate antiviral activity (~1.5-log inactivation within 120 min). Unexpectedly, although bulk g-C_3N_4 (prepared by thermal polycondensation of melamine [38]) has been found to effectively inactivate *E. coli* bacteria [39] and MS2 bacteriophages [12] under visible light irradiation, which outperformed other commonly used visible-light-responsive photocatalysts such as N-TiO_2 and Bi_2WO_6, it is for the first time to reveal that bulk g-C_3N_4 had no virucidal activity against human adenovirus. This could be due to a larger virus size (70–100 nm), a more complex capsid structure, and self-recovery of DNA viruses [40], which all result in a higher resistance of adenoviruses than MS2. Impressively, a significantly enhanced photocatalytic viral inactivation was observed once HTCC was integrated with O-g-C_3N_4 to form the O-g-C_3N_4/HTCC composites. Among them, O-g-C_3N_4/HTCC-2 showed the highest viral inactivation efficiency with complete inactivation of 5-log of HAdV-2

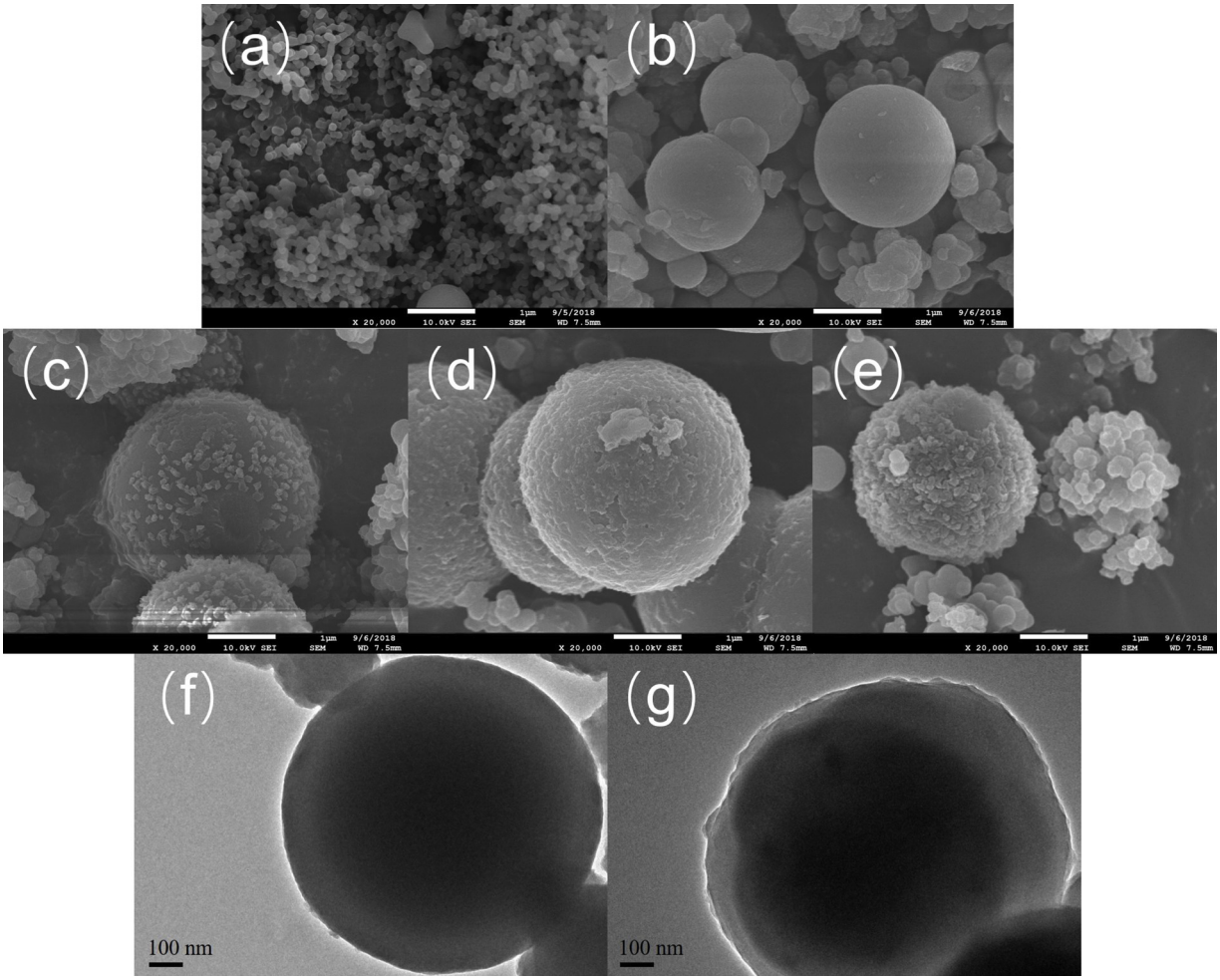

Fig. 2. SEM images of (a) HTCC, (b) O-g-C_3N_4, (c) O-g-C_3N_4/HTCC-1, (d) O-g-C_3N_4/HTCC-2, and (e) O-g-C_3N_4/HTCC-3, and TEM images of (f) O-g-C_3N_4 and (g) O-g-C_3N_4/HTCC-2.

within 120 min under visible light irradiation. A lower photocatalytic viral inactivation efficiency of O-g-C_3N_4/HTCC-1 and O-g-C_3N_4/HTCC-3 could be resulted from the insufficient and the excessive HTCC on O-g-C_3N_4. Insufficient HTCC coverage led to a small contact area between HTCC and O-g-C_3N_4, which was unfavorable for charge separation; while an excessive HTCC content caused its heavy aggregation and stacking to block light transmission and utilization, which also limited photocatalytic viral inactivation. In other words, the best photocatalytic virucidal performance of O-g-C_3N_4/HTCC-2 was derived from the uniform distribution of HTCC on the surface of O-g-C_3N_4 and strong visible light absorption, as confirmed by SEM, TEM, and UV–vis DRS.

O-g-C_3N_4/HTCC-2 was next selected for understanding the effects of complex water matrices on photocatalytic disinfection of HAdV-2. Key water quality parameters, including water temperature, pH, salinity and hardness, were evaluated. An increase of temperature from 4 °C to 37 °C, which represents environmental water temperature in natural and engineering systems, led to enhanced viral inactivation (Fig. 5b). Although the adenovirus is stable in this range of temperature, their structural proteins are sensitive to temperature changes, making them more susceptible to disinfection at higher temperature [41,42]. A decrease of pH from 8 to 5 promoted viral inactivation: all viruses were fully inactivated within 90 min at pH 5 (Fig. 5c). On one hand, electrostatic repulsion between the adenoviruses and O-g-C_3N_4/HTCC-2 could be reduced under acidic condition, corresponding to enhanced adsorption of viruses to the photocatalyst (Fig. 5c). On the other hand, the adenovirus has been found to be stable in pH 7–9 but less stable in lower pH of 5–7 [43]. Therefore, the acidic condition facilitates photocatalytic inactivation of adenoviruses on O-g-C_3N_4/HTCC-2. Photocatalytic viral inactivation was accelerated in the presence of salinity (NaCl) and hardness (Ca^{2+}) (Fig. 5d), of which the concentration of 1 mM represent most scenarios in drinking water [44]. This enhancement could be owing to i) metal cations are able to coordinate with the negatively charged N atoms in O-g-C_3N_4/HTCC-2 to facilitate charge separation [45], and ii) metal cations are able to neutralize/shield adenovirus surface charges to promote electrostatic attraction between adenoviruses and O-g-C_3N_4/HTCC-2 [46]. Besides, the presence of Ca^{2+} showed a greater enhancement of viral inactivation, probably because divalent cations could neutralize/shield virus surface charges much more effectively than monovalent cations. To further identify the improved photoactivity of O-g-C_3N_4/HTCC-2 by cations of Na^+/Ca^{2+} and to exclude the impact of Cl^-, Na_2SO_4 was employed to substitute NaCl with the same concentration of Na^+. The inactivation kinetics of HAdV-2 on O-g-C_3N_4/HTCC-2 in Na_2SO_4 solution was similar to that in NaCl solution (Fig. 5d), proposing an interesting speculation that photocatalytic viral inactivation by O-g-C_3N_4/HTCC-2 is dependent on cations but not on anions. To test the robustness and practicability of O-g-C_3N_4/HTCC-2 for viral disinfection, photocatalytic inactivation of HAdV-2 was also evaluated in real drinking water (Fig. 5e). The disinfection process was almost stagnant in the first 60 min of photocatalysis and the inactivation efficiency was much lower (only 1.8-log within 120 min), most likely due to natural organic matter competing for the active sites of photocatalysts and consuming the RS generated from photocatalysts [10]. Fortunately, O-g-C_3N_4/HTCC-2 could still totally inactivate adenoviruses (5-log

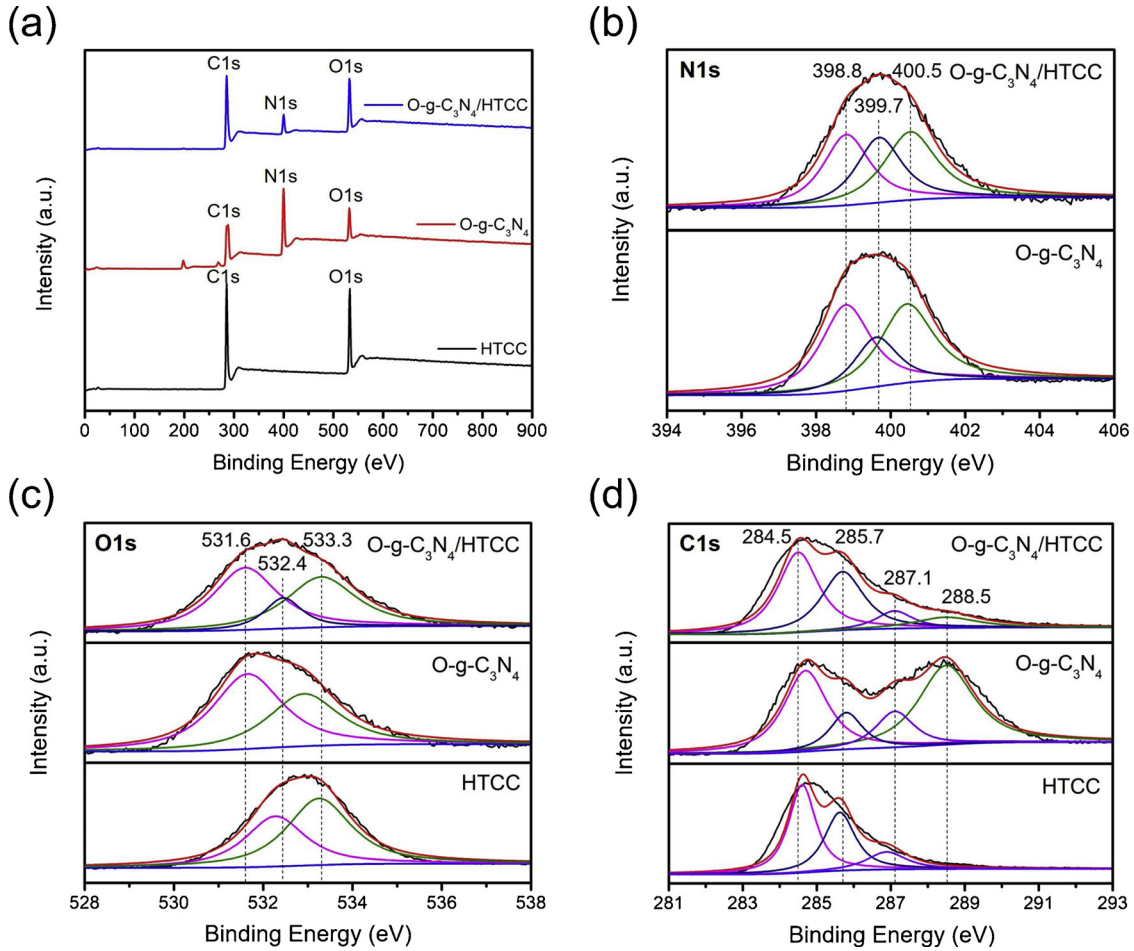

Fig. 3. (a) XPS survey spectra of HTCC, O-g-C_3N_4, and O-g-C_3N_4/HTCC-2, and high resolution XPS spectra of (b) N 1s, (c) O 1s, and (d) C 1s.

inactivation) in real drinking water with an extended during of 210 min under visible light irradiation, highlighting its promise for water disinfection in practice.

The photocatalyst stability over multiple disinfection cycles is also important for practical water disinfection. The O-g-C_3N_4/HTCC-2 photocatalyst was recovered after photocatalysis by centrifugation, and was introduced to a new suspension containing active HAdV-2 for the next cycle of disinfection. The results in Fig. 5f displayed that viruses were completely inactivated (5-log inactivation) in five cycles of disinfection (each cycle of 210 min) in real drinking water, declaring that O-g-C_3N_4/HTCC-2 is highly stable and robust for photocatalytic viral disinfection.

3.3. Enhanced photocatalytic mechanism

Generally, we can take advantage by constructing an effective heterojunction: i) more efficient charge separation, ii) rapid charge transfer, and iii) reduced charge recombination. All these features are

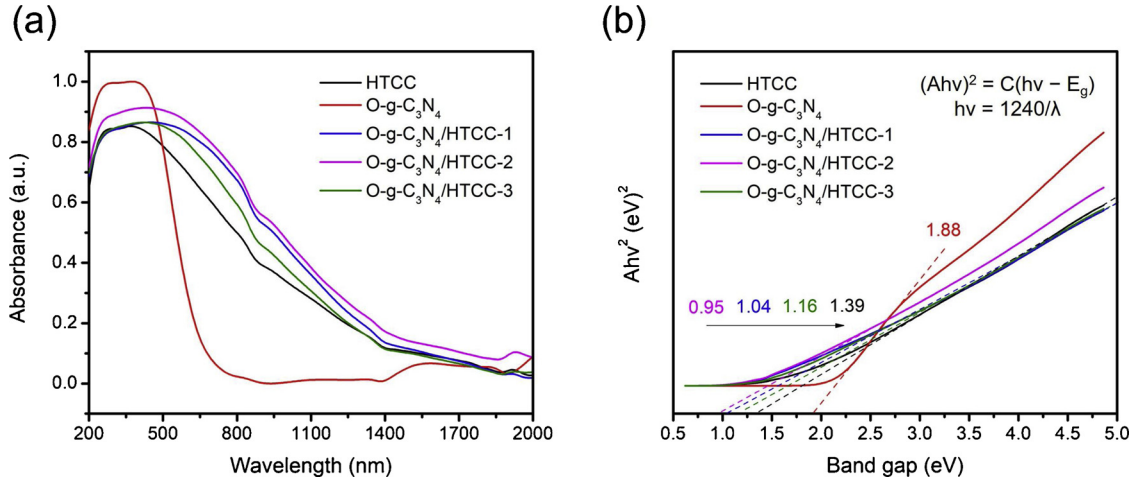

Fig. 4. (a) UV–vis DRS spectra and (b) band gap plots of HTCC, O-g-C_3N_4, and different O-g-C_3N_4/HTCC samples.

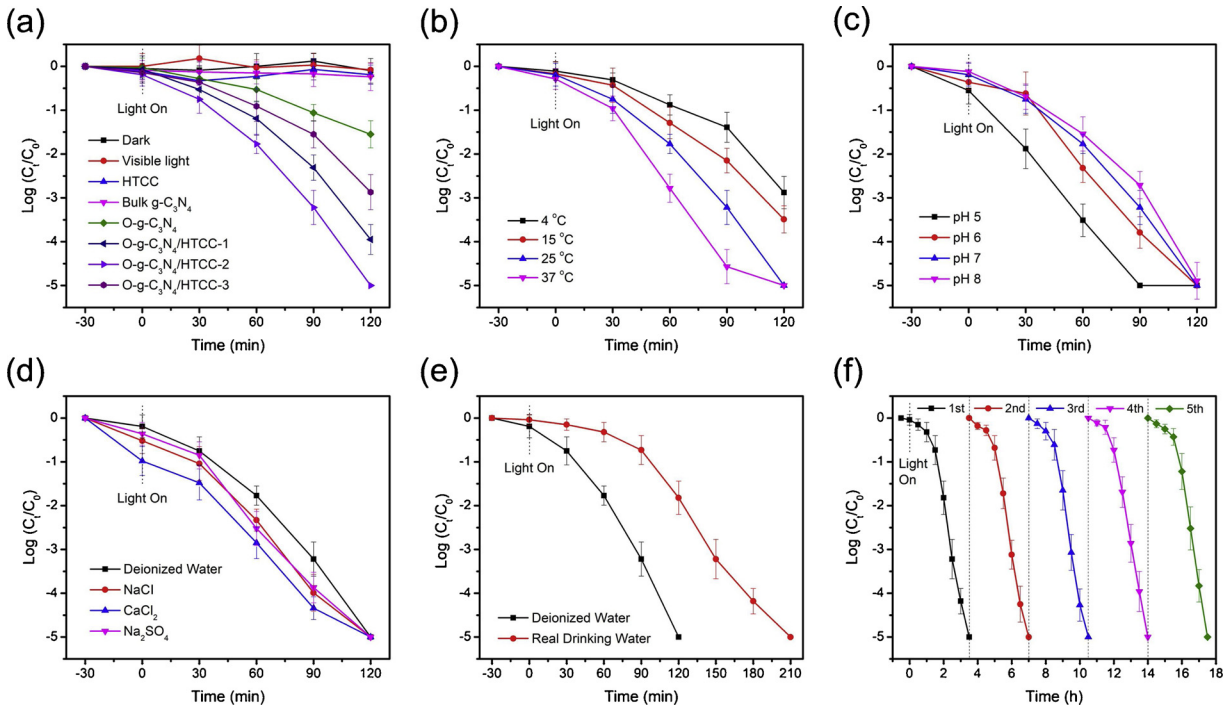

Fig. 5. (a) Photocatalytic inactivation of HAdV-2 by HTCC, O-g-C_3N_4, and different O-g-C_3N_4/HTCC samples under visible light irradiation; (b) effect of temperature, (c) effect of pH, (d) effect of inorganic ions, and (e) effect of real drinking water matrix on photocatalytic inactivation of HAdV-2 by O-g-C_3N_4/HTCC-2 under visible light irradiation; and (f) stability of O-g-C_3N_4/HTCC-2 for photocatalytic inactivation of HAdV-2 under visible light irradiation.

supposed to endow the heterojunction photocatalyst with enhanced photocatalytic performance. Hence, the mechanism of enhanced photocatalytic performance of O-g-C_3N_4/HTCC was systematically investigated for photogenerated charge separation, transfer, and recombination by PC, EIS, and PL.

The PC response is a valid technique to assess the interfacial charge separation efficiency in materials (Fig. 6a). All of our photocatalysts produced photocurrent under visible light irradiation, representing that they can respond to visible light to generate e^-/h^+ pairs. Obviously, the O-g-C_3N_4/HTCC composites presented much higher photocurrent densities than HTCC and O-g-C_3N_4 alone, manifesting that the heterojunctions between HTCC and O-g-C_3N_4 can enhance the separation of photogenerated charge carriers. Further, EIS was carried out to examine the charge transfer rate in the heterojunction system (Fig. 6b). It is well known that a smaller arc radius in the Nyquist plot signifies a lower charge transfer resistance, which favors a high charge transfer rate. As expected, the O-g-C_3N_4/HTCC composites had lower charge transfer resistances than HTCC and O-g-C_3N_4 alone, illustrating an improved electron transfer rate in the heterojunctions. The arc radius in the Nyquist plot of the heterojunctions was as follows: O-g-C_3N_4/HTCC-2 < O-g-C_3N_4/HTCC-1 < O-g-C_3N_4/HTCC-3, and faster charge transfer in the photocatalyst corresponds to enhanced charge separation, as indicated in the PC analysis. Additionally, PL was implemented to evaluate the recombination probability of photogenerated e^-/h^+ pairs in materials (Fig. 6c), and a stronger PL intensity refers to more radiative charge recombination [47]. Similarly, the formation of heterojunction between HTCC and O-g-C_3N_4 dramatically mitigated the charge recombination of HTCC and O-g-C_3N_4, and O-g-C_3N_4/HTCC-2 showed the lowest PL intensity compared to other heterojunction photocatalysts. All results above strongly support that coupling HTCC with O-g-C_3N_4 can enhance charge separation, accelerate charge transfer, and reduce radiative charge recombination, and thus improve photocatalytic activity owing to the formation of heterojunctions, especially for O-g-C_3N_4/HTCC-2. Consequently, it is not surprising that O-g-C_3N_4/HTCC-2 exhibited the best photocatalytic virucidal performance under visible light irradiation.

3.4. RS investigation and heterojunction determination

Photocatalytic water disinfection is believed to be induced by RS generated in photocatalysts, including photogenerated h^+ as well as reactive oxygen species (e.g. $^{\cdot}O_2^-$, $^{\cdot}OH$, and H_2O_2) which can pose

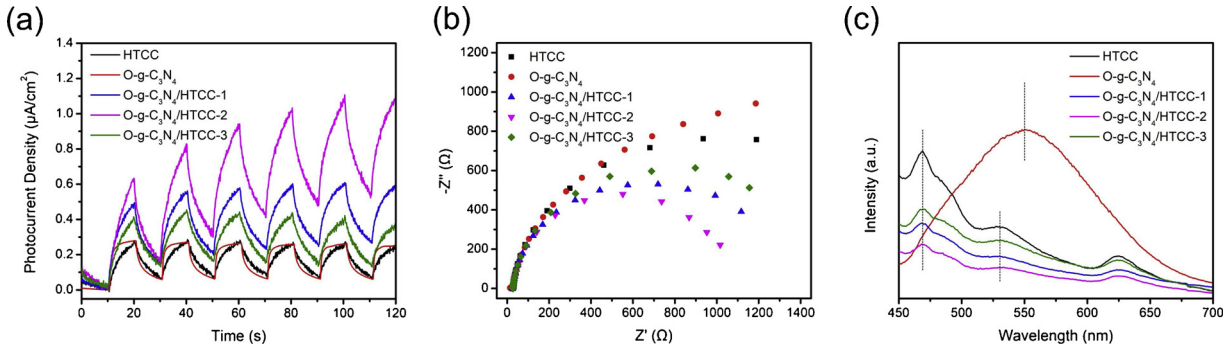

Fig. 6. (a) PC responses, (b) Nyquist plots of EIS, and (c) PL emission spectra of HTCC, O-g-C_3N_4, and different O-g-C_3N_4/HTCC samples.

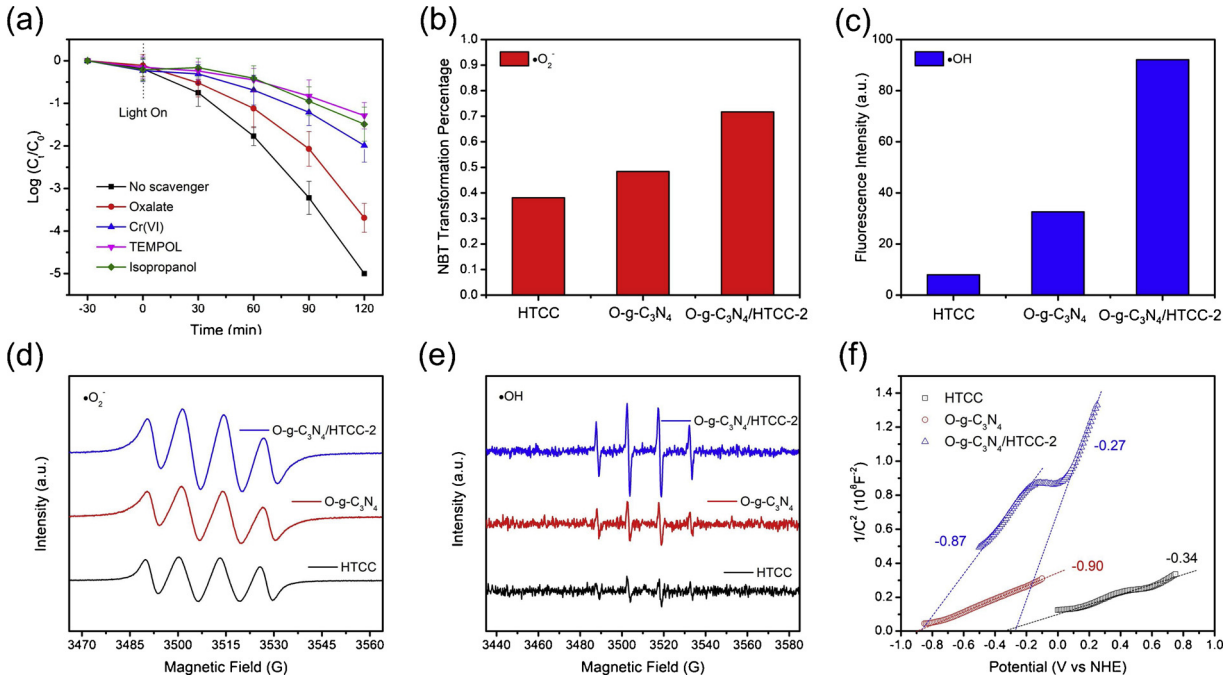

Fig. 7. (a) Photocatalytic inactivation of HAdV-2 by O-g-C_3N_4/HTCC-2 under visible light irradiation with the presence of different scavengers; (b) NBT reduction, (c) 2-HTA production, and ESR spectra of (d) DMPO-$^{\cdot}O_2^-$ in methanol and (e) DMPO-$^{\cdot}$OH in water by HTCC, O-g-C_3N_4, and O-g-C_3N_4/HTCC-2 under visible light irradiation; and (f) Mott-Schottky plots of HTCC, O-g-C_3N_4, and O-g-C_3N_4/HTCC-2 in the dark.

oxidative damage to pathogens. However, H_2O_2 at a concentration of up to 10 mg/L has been found to have no virucidal effect on adenoviruses [48]. As a result, H_2O_2 generated from O-g-C_3N_4/HTCC-2 with a much lower concentration had negligible inactivation for HAdV-2. The results of scavenger tests (Fig. 7a) showed that both photogenerated h^+ and e^- were involved in adenovirus inactivation, because the addition of oxalate, a h^+ scavenger, and Cr(VI), a e^- scavenger, obviously reduced the disinfection efficiency. Moreover, adenovirus disinfection was much more greatly inhibited in the presence of Cr(VI) than oxalate (2-log and 3.7-log inactivation *vs* 5-log inactivation when no scavenger was added), demonstrating a more major role of e^- in comparison of h^+ for viral inactivation. Notably, adenovirus inactivation was also significantly inhibited with the addition of either TEMPOL or isopropanol, stating that both $^{\cdot}O_2^-$ and $^{\cdot}$OH play an important role in this photocatalytic disinfection system. The effect of $HO_2^{\cdot}$ should be negligible because the pH of reaction solution (pH 7) was much higher than the pKa of $HO_2^{\cdot}/^{\cdot}O_2^-$ (pKa = 4.8) [49]. Therefore, $^{\cdot}O_2^-$ and $^{\cdot}$OH radicals were quantitatively analyzed by chemical probe transformation and ESR (Figs. 7b-e). More than 38% of NBT could be transformed by all photocatalysts, and the reduction of NBT gradually increased from HTCC, to O-g-C_3N_4, and to O-g-C_3N_4/HTCC-2 (Fig. 7b), suggesting all photocatalysts produced $^{\cdot}O_2^-$ under visible light irradiation (Fig. 7d). The production of $^{\cdot}$OH of the photocatalysts under visible light irradiation was quite different. HTCC and O-g-C_3N_4 produced little and moderate $^{\cdot}$OH, quantified by generating highly fluorescent 2-HTA from TA (Fig. 7c). In contrast, O-g-C_3N_4/HTCC-2 produced a much higher concentration of $^{\cdot}$OH (Fig. 7c). The result is consistent with the spectra of the $^{\cdot}$OH-DMPO adduct in Fig. 7e, indicating that the generation of $^{\cdot}$OH was negligible for HTCC but significant for O-g-C_3N_4/HTCC-2 under visible light irradiation. Undoubtedly, the formation of $^{\cdot}O_2^-$ and $^{\cdot}$OH was greatly promoted with the O-g-C_3N_4/HTCC-2 composite compared to HTCC and O-g-C_3N_4 alone (Fig. 7d–e), especially for $^{\cdot}$OH, benefited from the improved light harvesting, lowered electron transport resistance, enhanced charge separation, and reduced charge recombination.

To further reveal the capability of oxidation and reduction of the photocatalysts, the conduction band (CB) energy, valence band (VB) energy, and band energy alignment was determined based on Mott-Schottky measurements (Fig. 7f) and UV–vis DRS spectra (Fig. 4). The Mott-Schottky plots of all three samples presented a positive slope, proving that the photocatalysts were n-type semiconductors in which the CB potential is quite close to the flat-band potential [50–52]. The CB edge potential of HTCC and O-g-C_3N_4 was estimated to be −0.34 and −0.90 eV, respectively, which can directly reduce O_2 into $^{\cdot}O_2^-$ (−0.33 eV *vs* NHE) [53]. Based on the band gap of HTCC (1.39 eV) and O-g-C_3N_4 (1.88 eV) in Fig. 4b, their VB edge potential was calculated to be + 1.05 eV and + 0.98 eV, respectively, both of which cannot directly oxidize H_2O into $^{\cdot}$OH (+ 2.37 eV *vs* NHE). Thus, it is reasonable to speculate that the detected $^{\cdot}O_2^-$ and $^{\cdot}$OH were produced by reduction reactions of photogenerated e^- from CB rather than oxidation reactions of holes from VB. The increased production of $^{\cdot}$OH for O-g-C_3N_4 than HTCC might be due to the more negative CB potential, rendering electrons stronger reduction capability to facilitate multistep reduction of O_2 ($O_2 \rightarrow {}^{\cdot}O_2^- \rightarrow H_2O_2 \rightarrow {}^{\cdot}$OH).

Importantly, the Mott-Schottky plots clearly implied that a n-n heterojunction was formed between HTCC and O-g-C_3N_4 with the CB edge potential of −0.27 and −0.87 eV. The corresponding band energy alignment of O-g-C_3N_4/HTCC-2 was drawn in Fig. 8, suggesting the formation of a Z-scheme or Type II heterojunction. It is noted that although the effective charge separation can be achieved in the Type II heterojunction (Fig. 8b), the major limitation is that the oxidation and reduction power of photogenerated charge carriers is reduced upon charge transfer. This is because of electron transfer to the CB of HTCC with a less negative potential and hole transfer to the VB of O-g-C_3N_4 with a less positive potential. In contrast to the Type II heterojunction, Z-scheme is more attractive for photocatalysis because the stronger redox capability can be obtained (Fig. 8a). We measured a larger amount of $^{\cdot}O_2^-$ and especially $^{\cdot}$OH after the formation of heterojunction, and the results favor the argument of Z-scheme heterojunction formation in O-g-C_3N_4/HTCC-2 because a more negative CB edge potential of O-g-C_3N_4 with sufficient reduction power can favorably produce $^{\cdot}O_2^-$ and $^{\cdot}$OH from O_2.

Besides, a significant inhibition of viral inactivation with the addition of e^- scavenger in photocatalysis with O-g-C_3N_4/HTCC-2 also

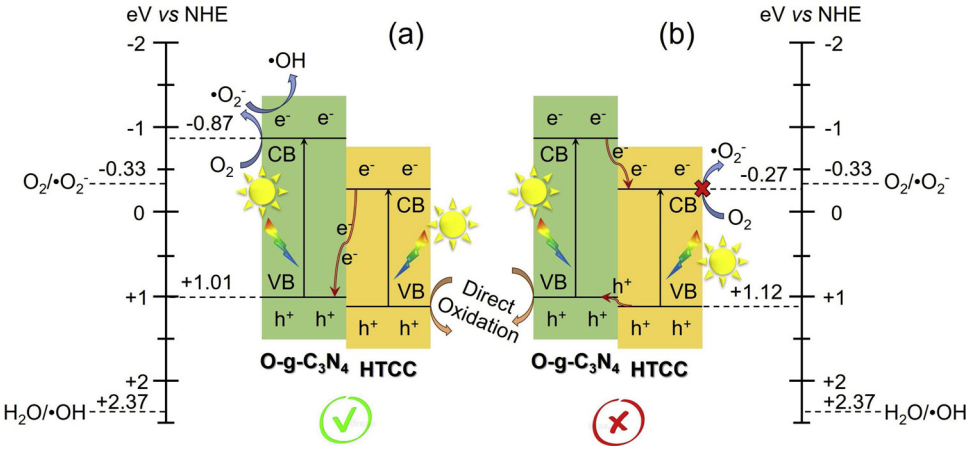

Fig. 8. Two possible heterojunctions of (a) Z-scheme and (b) Type II proposed for O-g-C_3N_4/HTCC-2 in photocatalysis.

supports the argument that $^{\cdot}O_2^-$ and ˙OH were formed via the reduction at CB (Fig. 7a). In addition, considering that ˙OH was derived from the reduction of $^{\cdot}O_2^-$, a similar extent of inhibition for viral disinfection in the presence of TEMPOL and isopropanol suggested that ˙OH instead of $^{\cdot}O_2^-$ could be the lethal agent for adenovirus inactivation. In contrast, $^{\cdot}O_2^-$ is considered as an essential antibacterial agent in the g-C_3N_4-based disinfection system [54], while ˙OH with a higher oxidation power and faster reaction kinetics is found to be a leading antiviral agent in this study, probably because the double-stranded DNA adenovirus possesses a more rigid capsid to defend viral particles against oxidative inactivation and the self-recovery of adenovirus after disinfection [40,55].

3.5. Viral particle damage

To better identify the destruction of viral particles during the photocatalytic disinfection by O-g-C_3N_4/HTCC-2, the morphology change of HAdV-2 was visualized by TEM (Fig. 9). Before photocatalytic disinfection, HAdV-2 exhibited a well-preserved icosahedral shape with an integral protein shell with a size of ˜80 nm (Fig. 9a). As the disinfection proceeded, it was observed that HAdV-2 became distorted and the viral capsid was ruptured with the presence of holes (Fig. 9b). The capsid is considered as not only an excellent protection for viral genes but also an important determinant for viral infectivity because of the specific recognition of cells with viral proteins (i.e., coxsackievirus and adenovirus receptor on the cells binds to the knob domain of the fiber protein of HAdV-2) [56]. The capsid destruction would lead to the leakage of genes, inactivation of genes, and the loss of infectivity/pathogenicity. Finally, at the end of disinfection of 120 min, no intact HAdV-2 could be found and only virus debris was observed (Fig. 9c), claiming severe lethal damage towards HAdV-2 induced by O-g-C_3N_4/HTCC-2 under visible light irradiation.

3.6. Toxicity assessment

For the practical application of our photocatalysts for drinking water treatment, the toxicity of the photocatalysts, including HTCC, O-g-C_3N_4, O-g-C_3N_4/HTCC-2, was tested through the XTT assay with human A549 cells. As shown in Fig.10, all samples displayed a negligible toxicity to human cells within a range of photocatalyst loadings. The cell viability slightly decreased with all samples at the high concentration of 150 μg/mL. Even at such a high photocatalyst loading, over 85% of the human A549 cells remained alive, announcing that not only HTCC and O-g-C_3N_4 but also the heterostructural O-g-C_3N_4/HTCC-2 had excellent biocompatibility and negligible cytotoxicity towards human cells. This “green” feature of the heterojunction photocatalyst may be originated from its metal-free nature (i.e. C, N, O elements) and chemical stability.

Herein, the developed novel heterojunction photocatalysts of O-g-C_3N_4 and HTCC possess the following unique advantages: i) the materials can be synthesized via a facile and sustainable solvothermal-hydrothermal approach at low temperature of 180 °C; ii) the materials are metal-free and only contain earth-abundant elements, i.e. C, N and O, which reduce the cost of photocatalyst fabrication and avoid the risk of metal leaching into treated water; iii) the materials can effectively utilize visible light for sustainable water treatment; iv) the materials show excellent and robust photocatalytic performance for inactivating human adenovirus, which is well-known to be resistant in conventional

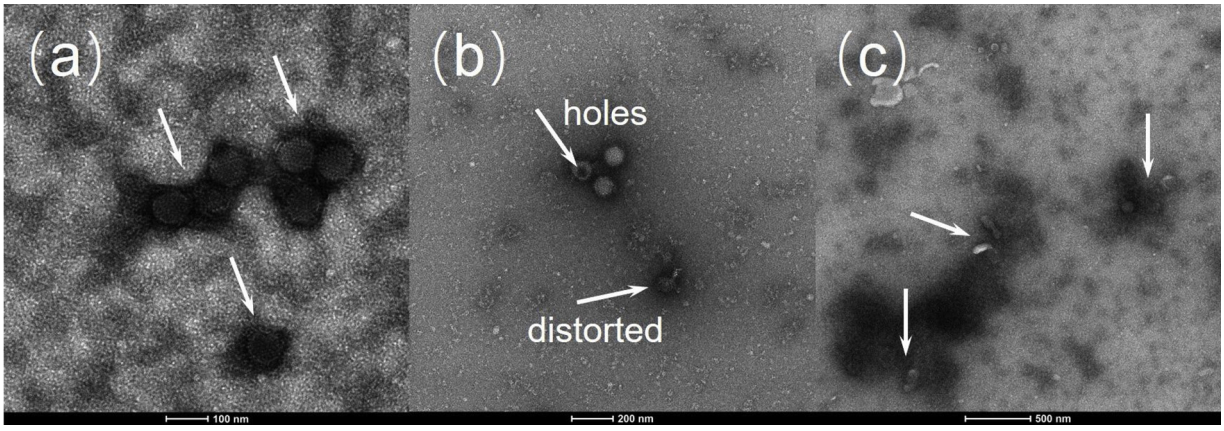

Fig. 9. TEM images of HAdV-2 treated with O-g-C_3N_4/HTCC-2 for (a) 0 h, (b) 1 h, and (c) 2 h under visible light irradiation.

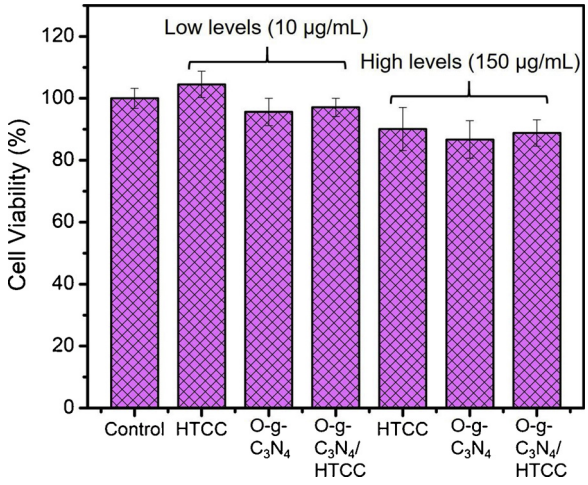

Fig. 10. Cytotoxic effects of HTCC, O-g-C_3N_4, and O-g-C_3N_4/HTCC-2 at different levels on human lung carcinoma cells (A549).

water disinfection processes (e.g., UV); and vi) the materials are biocompatible thus promote safe water treatment. All these merits endow the heterojunction photocatalysts promise for water disinfection in practice. Future studies are encouraged to shorten the material synthesis time with new improved methods, and to immobilize the material on the substrates or to couple the material in the reactors for point-of-use water disinfection.

4. Conclusion

In summary, a series of novel metal-free heterojunction photocatalysts, O-g-C_3N_4/HTCC microspheres, were successfully developed by a facile two-step approach at low temperature. Among them, O-g-C_3N_4/HTCC-2 with a desired amount of HTCC had a uniform surface coverage on O-g-C_3N_4 and strong visible light absorption. Satisfactorily, O-g-C_3N_4/HTCC-2 showed the best virucidal activity for pathogen HAdV-2, namely complete 5-log inactivation within 120 min, under visible light irradiation. The enhanced viral inactivation performance of O-g-C_3N_4/HTCC-2 was attributed to the successful construction of Z-scheme heterojunction that can improve charge separation, accelerate charge transfer, and reduce charge recombination. Moreover, the Z-scheme facilitated the production of the leading antiviral agent, i.e. $^{\cdot}OH$, and resulted in the lethal rupture of rigid capsid of HAdV-2. Our heterojunction photocatalyst holds promise for effective, sustainable, environmentally friendly, and potentially low-cost water disinfection, and the photocatalytic system can be used for small-scale water treatment in rural areas, developing countries, and regions after natural disasters to provide safe drinking water.

Acknowledgements

This study was supported by the National Natural Science Foundation of China (No. 91547105 and 51779076); the Foundation for Innovative Research Groups of the National Natural Science Foundation of China (No. 51421006); the Priority Academic Program Development of Jiangsu Higher Education Institutions (PAPD); the Six Talent Peaks Project in Jiangsu Province (2016-JNHB-007); the 333 Talent Project Foundation of Jiangsu Province; the Fundamental Research Funds for the Central Universities (2018B41714 and 2018B47814) and the Postgraduate Research & Practice Innovation Program of Jiangsu Province (KYZZ16_0291). This study was also supported by National Science Foundation grant (CHE-1807617) and US Department of Agriculture-National Institute of Food and Agriculture grant (USDA-NIFA Grant 2017-67021-26602).

Appendix A. Supplementary data

Supplementary material related to this article can be found, in the online version, at doi:https://doi.org/10.1016/j.apcatb.2019.02.009.

References

[1] K.E. Gibson, Viral pathogens in water: occurrence, public health impact, and available control strategies, Curr. Opin. Virol. 4 (2014) 50–57.
[2] A.M. Gall, B.J. Marinas, Y. Lu, J.L. Shisler, Waterborne viruses: a barrier to safe drinking water, PLoS Pathog. 11 (2015) e1004867.
[3] W.A. Hijnen, G.M. Suylen, J.A. Bahlman, A. Brouwer-Hanzens, G.J. Medema, GAC adsorption filters as barriers for viruses, bacteria and protozoan (oo)cysts in water treatment, Water Res. 44 (2010) 1224–1234.
[4] D. Berman, J.C. Hoff, Inactivation of simian rotavirus SA11 by chlorine, chlorine dioxide, and monochloramine, Appl. Environ. Microbiol. 48 (1984) 317–323.
[5] K. Sirikanchana, J.L. Shisler, B.J. Marinas, Effect of exposure to UV-C irradiation and monochloramine on adenovirus serotype 2 early protein expression and DNA replication, Appl. Environ. Microbiol. 74 (2008) 3774–3782.
[6] D. Li, A.Z. Gu, M. He, H.C. Shi, W. Yang, UV inactivation and resistance of rotavirus evaluated by integrated cell culture and real-time RT-PCR assay, Water Res. 43 (2009) 3261–3269.
[7] V.K. Sharma, R. Zboril, T.J. McDonald, Formation and toxicity of brominated disinfection byproducts during chlorination and chloramination of water: a review, J. Environ. Sci. Health B 49 (2014) 212–228.
[8] A.M. Gall, J.L. Shisler, B.J. Marinas, Analysis of the viral replication cycle of adenovirus serotype 2 after inactivation by free chlorine, Environ. Sci. Technol. 49 (2015) 4584–4590.
[9] M. Cho, H. Chung, W. Choi, J. Yoon, Different inactivation behaviors of MS-2 phage and *Escherichia coli* in TiO_2 photocatalytic disinfection, Appl. Environ. Microbiol. 71 (2005) 270–275.
[10] C. Zhang, Y. Li, D. Shuai, W. Zhang, L. Niu, L. Wang, H. Zhang, Visible-light-driven, water-surface-floating antimicrobials developed from graphitic carbon nitride and expanded perlite for water disinfection, Chemosphere 208 (2018) 84–92.
[11] C. Zhang, Y. Li, D. Shuai, Y. Shen, D. Wang, Progress and challenges in photocatalytic disinfection of waterborne viruses: a review to fill current knowledge gaps, Chem. Eng. J. 355 (2019) 399–415.
[12] Y. Li, C. Zhang, D. Shuai, S. Naraginti, D. Wang, W. Zhang, Visible-light-driven photocatalytic inactivation of MS2 by metal-free g-C_3N_4: virucidal performance and mechanism, Water Res. 106 (2016) 249–258.
[13] W.J. Ong, L.L. Tan, Y.H. Ng, S.T. Yong, S.P. Chai, Graphitic carbon nitride (g-C_3N_4)-based photocatalysts for artificial photosynthesis and environmental remediation: are we a step closer to achieving sustainability? Chem. Rev. 116 (2016) 7159–7329.
[14] C. Zhang, Y. Li, W. Zhang, P. Wang, C. Wang, Metal-free virucidal effects induced by g-C_3N_4 under visible light irradiation: statistical analysis and parameter optimization, Chemosphere 195 (2018) 551–558.
[15] Z. Hu, Z. Shen, J.C. Yu, Converting carbohydrates to carbon-based photocatalysts for environmental treatment, Environ. Sci. Technol. 51 (2017) 7076–7083.
[16] Z. Hu, G. Liu, X. Chen, Z. Shen, J.C. Yu, Enhancing charge separation in metallic photocatalysts: a case study of the conducting molybdenum dioxide, Adv. Funct. Mater. 26 (2016) 4445–4455.
[17] T. Wang, Z. Jiang, T. An, G. Li, H. Zhao, P.K. Wong, Enhanced visible-light-driven photocatalytic bacterial inactivation by ultrathin carbon-coated magnetic cobalt ferrite nanoparticles, Environ. Sci. Technol. 52 (2018) 4774–4784.
[18] Y. Wang, H. Wang, F. Chen, F. Cao, X. Zhao, S. Meng, Y. Cui, Facile synthesis of oxygen doped carbon nitride hollow microsphere for photocatalysis, Appl. Catal. B 206 (2017) 417–425.
[19] J. Hewitt, M. Leonard, G.E. Greening, G.D. Lewis, Influence of wastewater treatment process and the population size on human virus profiles in wastewater, Water Res. 45 (2011) 6267–6276.
[20] L. Ogorzaly, S. Bonot, B.E. Moualij, W. Zorzi, H.M. Cauchie, Development of a quantitative immunocapture real-time PCR assay for detecting structurally intact adenoviral particles in water, J. Virol. Methods 194 (2013) 235–241.
[21] S. Meister, M.E. Verbyla, M. Klinger, T. Kohn, Variability in disinfection resistance between currently circulating *Enterovirus B* serotypes and strains, Environ. Sci. Technol. 52 (2018) 3696–3705.
[22] K. Sirikanchana, J.L. Shisler, B.J. Marinas, Inactivation kinetics of adenovirus serotype 2 with monochloramine, Water Res. 42 (2008) 1467–1474.
[23] C. San Martin, Latest insights on adenovirus structure and assembly, Viruses 4 (2012) 847–877.
[24] B. Vazquez-Bravo, K. Goncalves, J.L. Shisler, B.J. Marinas, Adenovirus replication cycle disruption from exposure to polychromatic ultraviolet irradiation, Environ. Sci. Technol. 52 (2018) 3652–3659.
[25] P.C. Nagajyothi, S.J. Cha, I.J. Yang, T.V. Sreekanth, K.J. Kim, H.M. Shin, Antioxidant and anti-inflammatory activities of zinc oxide nanoparticles synthesized using *Polygala tenuifolia* root extract, J. Photochem. Photobiol. B 146 (2015) 10–17.
[26] M. Reis Ede, A.A. Rezende, P.F. Oliveira, H.D. Nicolella, D.C. Tavares, A.C. Silva, N.O. Dantas, M.A. Spano, Evaluation of titanium dioxide nanocrystal-induced genotoxicity by the cytokinesis-block micronucleus assay and the *Drosophila* wing spot test, Food Chem. Toxicol. 96 (2016) 309–319.
[27] Y. Huang, Y. Liang, Y. Rao, D. Zhu, J.J. Cao, Z. Shen, W. Ho, S.C. Lee, Environment-friendly carbon quantum dots/$ZnFe_2O_4$ photocatalysts: characterization, biocompatibility, and mechanisms for NO removal, Environ. Sci. Technol. 51 (2017)

2924–2933.
[28] Y. Yuan, L. Yin, S. Cao, L. Gu, G. Xu, P. Du, H. Chai, Y. Liao, C. Xue, Microwave-assisted heating synthesis: a general and rapid strategy for large-scale production of highly crystalline g-C_3N_4 with enhanced photocatalytic H_2 production, Green Chem. 16 (2014) 4663–4668.
[29] L. Ming, H. Yue, L. Xu, F. Chen, Hydrothermal synthesis of oxidized g-C_3N_4 and its photocatalytic activity regulation, J. Mater. Chem. A 2 (2014) 19145–19149.
[30] X. Wu, F. Chen, X. Wang, H. Yu, In situ one-step hydrothermal synthesis of oxygen-containing groups-modified g-C_3N_4 for the improved photocatalytic H_2-evolution performance, Appl. Surf. Sci. 427 (2018) 645–653.
[31] A. Nezamzadeh-Ejhieh, M. Kabiri-Samani, Effective removal of Ni(II) from aqueous solutions by modification of nano particles of clinoptilolite with dimethylglyoxime, J. Hazard. Mater. 260 (2013) 339–349.
[32] Z. Zeng, X. Quan, H. Yu, S. Chen, Y. Zhang, H. Zhao, S. Zhang, Carbon nitride with electron storage property: enhanced exciton dissociation for high-efficient photocatalysis, Appl. Catal. B 236 (2018) 99–106.
[33] J. Tian, J. Chen, J. Liu, Q. Tian, P. Chen, Graphene quantum dot engineered nickel-cobalt phosphide as highly efficient bifunctional catalyst for overall water splitting, Nano Energy 48 (2018) 284–291.
[34] Y. Cui, Z. Ding, X. Fu, X. Wang, Construction of conjugated carbon nitride nanoarchitectures in solution at low temperatures for photoredox catalysis, Angew. Chem. Int. Ed. Engl. 51 (2012) 11814–11818.
[35] Z. Huang, J. Song, L. Pan, Z. Wang, X. Zhang, J. Zou, W. Mi, X. Zhang, L. Wang, Carbon nitride with simultaneous porous network and O-doping for efficient solar-energy-driven hydrogen evolution, Nano Energy 12 (2015).
[36] G. Li, X. Liu, H. Zhang, P.K. Wong, T. An, W. Zhou, B. Li, H. Zhao, Adenovirus inactivation by in situ photocatalytically and photoelectrocatalytically generated halogen viricides, Chem. Eng. J. 253 (2014) 538–543.
[37] B. Guo, S.D. Snow, B.J. Starr, I. Xagoraraki, V.V. Tarabara, Photocatalytic inactivation of human adenovirus 40: effect of dissolved organic matter and prefiltration, Sep. Purif. Technol. 193 (2018) 193–201.
[38] S. Yan, Z. Li, Z. Zou, Photodegradation performance of g-C_3N_4 fabricated by directly heating melamine, Langmuir 25 (2009) 10397–10401.
[39] J. Huang, W. Ho, X. Wang, Metal-free disinfection effects induced by graphitic carbon nitride polymers under visible light illumination, Chem. Commun. 50 (2014) 4338–4340.
[40] S.K. Weller, J.A. Sawitzke, Recombination promoted by DNA viruses: phage λ to herpes simplex virus, Annu. Rev. Microbiol. 68 (2014) 237–258.
[41] M.A. Page, J.L. Shisler, B.J. Marinas, Kinetics of adenovirus type 2 inactivation with free chlorine, Water Res. 43 (2009) 2916–2926.
[42] B. Prevost, M. Goulet, F.S. Lucas, M. Joyeux, L. Moulin, S. Wurtzer, Viral persistence in surface and drinking water: suitability of PCR pre-treatment with intercalating dyes, Water Res. 91 (2016) 68–76.
[43] H.S. Ginsberg, Characteristics of the new respiratory viruses (adenoviruses) II. Stability to temperature and pH alterations, Proc. Soc. Exp. Biol. Med. 93 (1956) 48–52.
[44] J.F. Schijven, S.M. Hassanizadeh, Removal of viruses by soil passage: overview of modeling, processes, and parameters, Crit. Rev. Environ. Sci. Technol. 30 (2000) 49–127.
[45] H. Gao, S. Yan, J. Wang, Z. Zou, Inorganic ions promoted photocatalysis based on polymer photocatalyst, Appl. Catal. B 158-9 (2014) 321–328.
[46] K. Wong, B. Mukherjee, A.M. Kahler, R. Zepp, M. Molina, Influence of inorganic ions on aggregation and adsorption behaviors of human adenovirus, Environ. Sci. Technol. 46 (2012) 11145–11153.
[47] Q. Zheng, D.P. Durkin, J.E. Elenewski, Y. Sun, N.A. Banek, L. Hua, H. Chen, M.J. Wagner, W. Zhang, D. Shuai, Visible-light-responsive graphitic carbon nitride: rational design and photocatalytic applications for water treatment, Environ. Sci. Technol. 50 (2016) 12938–12948.
[48] S. Bounty, R.A. Rodriguez, K.G. Linden, Inactivation of adenovirus using low-dose UV/H_2O_2 advanced oxidation, Water Res. 46 (2012) 6273–6278.
[49] Q. Zheng, E. Xu, E. Park, H. Chen, D. Shuai, Looking at the overlooked hole oxidation: photocatalytic transformation of organic contaminants on graphitic carbon nitride under visible light irradiation, Appl. Catal. B 240 (2019) 262–269.
[50] G. Dong, K. Zhao, L. Zhang, Carbon self-doping induced high electronic conductivity and photoreactivity of g-C_3N_4, Chem. Commun. 48 (2012) 6178–6180.
[51] L. Li, J. Yan, T. Wang, Z.J. Zhao, J. Zhang, J. Gong, N. Guan, Sub-10 nm rutile titanium dioxide nanoparticles for efficient visible-light-driven photocatalytic hydrogen production, Nat. Commun. 6 (2015) 5881.
[52] D. Xia, W. Wang, R. Yin, Z. Jiang, T. An, G. Li, H. Zhao, P.K. Wong, Enhanced photocatalytic inactivation of *Escherichia coli* by a novel Z-scheme g-C_3N_4/m-Bi_2O_4 hybrid photocatalyst under visible light: the role of reactive oxygen species, Appl. Catal. B 214 (2017) 23–33.
[53] Q. Zheng, H. Shen, D. Shuai, Emerging investigators series: advances and challenges of graphitic carbon nitride as a visible-light-responsive photocatalyst for sustainable water purification, Environ. Sci.: Water Res Technol. 3 (2017) 982–1001.
[54] M. Hayyan, M.A. Hashim, I.M. AlNashef, Superoxide ion: generation and chemical implications, Chem. Rev. 116 (2016) 3029–3085.
[55] M.D. Weitzman, C.T. Carson, R.A. Schwartz, C.E. Lilley, Interactions of viruses with the cellular DNA repair machinery, DNA Repair 3 (2004) 1165–1173.
[56] J.C. Grieger, S. Snowdy, R.J. Samulski, Separate basic region motifs within the adeno-associated virus capsid proteins are essential for infectivity and assembly, J. Virol. 80 (2006) 5199–5210.